Biosensors and Bioelectronics: X 15 (2023) 100413

Contents lists available at ScienceDirect

Biosensors and Bioelectronics: X

journal homepage: www.journals.elsevier.com/biosensors-and-bioelectronics-x

Detection of anti-SARS CoV-2 antibodies in human serum by means of Bloch surface waves on 1D photonic crystal biochips☆

Agostino Occhicone [a,b,*], Alberto Sinibaldi [a,b], Daniele Chiappetta [a,b], Paola Di Matteo [a,b], Tommaso Pileri [a], Norbert Danz [c], Frank Sonntag [d], Peter Munzert [c], Matteo Allegretti [e], Valentina De Pascale [e], Chiara Mandoj [e], Francesco Michelotti [a,b]

[a] SAPIENZA Università di Roma, Department of Basic and Applied Sciences for Engineering, Via A. Scarpa, 16, 00161, Roma, Italy
[b] Italian Institute of Technology (IIT), Center for Life Nano and Neuro Science, Viale Regina Elena 291, 00161, Rome, Italy
[c] Fraunhofer Institute for Applied Optics and Precision Engineering (IOF), A.-Einstein-Str. 7, 07745, Jena, Germany
[d] Fraunhofer Institute for Material and Beam Technology (IWS), Winterbergstr. 28, 01277, Dresden, Germany
[e] Translational Oncology Research Unit, IRCCS Regina Elena National Cancer Institute, Rome, Italy

ARTICLE INFO

Keywords:
SARS-CoV-2
Biosensors
One-dimensional photonic crystals
Bloch surface waves

ABSTRACT

This study presents the development and characterization of a disposable biochip for the detection of antibodies against the SARS-CoV-2 spike protein, a well-known target for vaccine and therapeutic development. This biochip is based on a one-dimensional photonic crystal (1DPC) deposited on a plastic substrate and designed to sustain Bloch surface waves (BSW) in the visible range. The experimental phase was carried out using the biochip in conjunction with a custom-made optical read-out platform capable of real-time refractometric detection and fluorescence-based end-point measurements. Our biochip was functionalized by immobilizing the receptor-binding domain of the spike protein onto the surface using a silanization process. Human serum samples, including a negative control and a positive sample from a recovered COVID-19 patient, were tested on the biochip. The experimental results show that the biochip discriminates between positive and negative samples in a label-free refractometric mode down to a 1:10 dilution of the sera and in quantum dot amplified refractometric and fluorescence mode down to 1:100 dilution. The results demonstrate the potential of the disposable biochip for sensitive and specific detection of COVID-19 antibodies.

1. Introduction

The SARS-CoV-2 RNA virus was discovered in Wuhan, China, by the end of 2019 and rapidly evolved into a global pandemic (WHO, s.d.; Singhal, 2020; Coronaviridae Study Group of the International Committee on Taxonomy of Viruses, 2020). The molecular polymerase chain reaction (PCR) was initially used to detect viral RNA in patient fluids like nasal and pharyngeal swabs, determining contagion potential (Han et al., 2021). However, due to RNA sequence changes, certain RT-PCR-based tests couldn't detect the SARS-CoV-2 Omicron variant, unless they underwent a specific reconfiguration (Ascoli C.A., 2021; Chen et al., 2022; Duffy, 2018). Infected patients produce antibodies against SARS-CoV-2 proteins, present in body fluids such as blood, serum, plasma, and saliva (Chen et al., 2022; Yüce et al., 2021; Perveen et al., 2023; Naqvi et al., 2020). Serological tests have been increasingly employed to understand infection rates and assess immunity status (Coronaviridae Study Group of the International Committee on Taxonomy of Viruses, 2020; Yüce et al., 2021; Perveen et al., 2023; Shafie et al., 2023; Chen et al., 2020; Lin et al., 2020).

Detecting low concentrations of specific virus-fighting antibodies (IgG, IgM) has become crucial in managing the ongoing pandemic and potential future ones (Chen et al., 2022; Yüce et al., 2021; Perveen et al., 2023; Naqvi et al., 2020). An ideal solution is a cost-effective, rapid on-site test with high sensitivity and specificity, requiring minimal user intervention [e.g., little hands-on time and low risk]. Lateral flow immunoassays (LFIAs) detect viral antigens or antibodies but have limited sensitivity, missing early infections when the virus can be transmitted (Chen et al., 2020; Lin et al., 2020; Mak et al., 2020; Peeling et al., 2021). In contrast, enzyme-linked immunosorbent assays (ELISA) and immune-chemiluminescence assays (CLIA) are highly sensitive and

☆ Electronic Supplementary Information (SI) available See DOI: 10.1039/x0xx00000x.

* Corresponding author. SAPIENZA Università di Roma, Department of Basic and Applied Sciences for Engineering, Via A. Scarpa, 16, 00161, Roma, Italy.
E-mail address: agostino.occhicone@uniroma1.it (A. Occhicone).

https://doi.org/10.1016/j.biosx.2023.100413
Received 12 June 2023; Received in revised form 9 October 2023; Accepted 19 October 2023
Available online 3 November 2023

reliable but require longer response times (4–6 h) and specialized platforms (Chen et al., 2022; Yüce et al., 2021; Perveen et al., 2023).

In this study, we showcase the effectiveness of a rapid serologic test utilizing an optical read-out platform and disposable nano-photonic biochips with a one-dimensional photonic crystal (1DPC), which were developed in previous works for other applications (Konopsky and Alieva, 2007; Yeh et al., 1977; Yeh and Yariv, 1978; Joannopoulos et al., 2008; Meade et al., 1991; Vinogradov et al., 2010; Sinibaldi et al., 2013). The test is designed for the detection of anti-SARS-CoV-2 antibodies. As the receptor-binding domain (RBD) of the spike protein is poorly conserved between SARS-CoVs and other pathogenic human coronaviruses, the RBD represents the main antigen for detecting CoV-specific antibodies in people (Premkumar et al., 2020). 1DPC biosensors sustain Bloch surface waves (BSW) (Konopsky and Alieva, 2007; Shinn and Robertson, 2005; Liscidini and Sipe, 2007; Guo et al., 2010; Qiao et al., 2010; Guo et al., 2008; Paeder et al., 2011; Farmer et al., 2012; Toma et al., 2013; Santi et al., 2013; Sreekanth et al., 2013; Rodriguez et al., 2014; Degli-Eredi et al., 2018; Petrova et al., 2019; Kalas et al., 2021; Robertson et al., 2020), offering an alternative to surface plasmon polariton (SPP)-based biosensors on noble metal surfaces (Sinibaldi, et al., 2012; Homola et al., 1999). Like SPP sensors (Raether, 1986; Danz et al., 2011; Michelotti et al., 2009), BSW sensors can detect changes in refractive index at their sensitive surface with high sensitivity, in a label-free manner. Additionally, fluorescence-based sensing schemes allow emitters in proximity to the 1DPC to couple with the BSW mode, enhancing excitation rates and BSW-coupled emission for novel fluorescence detection and biosensing (Sinibaldi et al., 2014, 2018; Ye et al., 1999; Ye and Ishikawa, 2008; Liscidini et al., 2009). The coupling strength is influenced by the local density of optical states, which is relatively large for BSW due to strong localization at the 1DPC surface (Michelotti and Sepe, 2019; Sepe et al., 2019). This coupling links emitted polarization with molecular orientation (Choudhury et al., 2015; Michelotti and Sepe, 2019; Sepe et al., 2019; Lakowicz, 2006).

2. Materials and methods

2.1. Disposable biochip

The experimental assays were carried out by means of disposable biochips constituted of a dielectric 1DPC deposited by plasma ion-assisted evaporation onto an optical quality plastic substrate made of a cyclic olefin copolymer (TOPAS 5013 LS), as sketched in Fig. 1 (a) (Munzert et al., 2017). The dielectric materials used for the fabrication of the 1DPC were SiO_2 (silica), Ta_2O_5 (tantala) and TiO_2 (titania). As shown in Fig. 1 (b), starting from the substrate side, the 1DPC was constituted of a first silica matching layer, a periodic part with two tantala/silica bilayers and a topping thin titania/silica bilayer (Sinibaldi et al., 2017). The thicknesses were $d_{SiO_2} = 275\ nm$, $d_{Ta_2O_5} = 120\ nm$ for the periodic part and $d_{TiO_2} = 20\ nm$, $d_{SiO_2} = 20\ nm$ for the topping layers. The refractive indices of the layers were: $(TiO_2)\ 2.280 + i1.8 \times 10^{-3}$, $(SiO_2)\ 1.474 + i5 \times 10^{-6}$, $(Ta_2O_5)\ 2.106 + i5 \times 10^{-5}$ at $\lambda_{LF} = 673\ nm$ (Munzert et al., 2017).

The 1DPC was designed to sustain Bloch surface waves (BSW) in the visible range when operating with protein solutions in aqueous environment ($n_L = 1.330$, the calculated photonic band structure and BSW dispersion is provided in section S.1 in the Supplementary Information (SI)) (Munzert et al., 2017). As shown in Fig. 1 (a), the plastic substrate had a prism shaped cross section that allowed operating under the total internal reflection (TIR) conditions needed to excite the BSW in the Kretschmann - Raether configuration (Kretschmann and Raether, 1968).

2.2. The read-out platform

The optical read-out system (Occhicone et al., 2021; Sinibaldi et al., 2015, 2017) can analyze the interaction kinetics in real time with accuracy, specificity and reliability. The novelty of the proposed approach lies in the particular photonic configuration that combines a label-free and real time refractometric detection scheme (LF) (Guo, et al., 2010) with a fluorescence-based end-point assay (FLR) (details in section S.2 of the SI) (Sinibaldi et al., 2017). In the LF and FLR operation modes the biochip is illuminated under TIR conditions by means of two different laser diodes emitting at λ_{LF} and $\lambda_{EXC} = 637nm$, respectively. Both lasers are TE polarized. The laser beams are shaped by means of cylindrical optics so as to illuminate a strip (Fig. 1 (a)) at the surface of the biochip. As sketched in Fig. 1 (c), and discussed in detail in the SI, the LF laser is focused in a $\sim 6\ deg$ angular range to carry out angularly resolved reflectance measurements, while the FLR laser is focused in a $\sim 1\ deg$ range to increase the coupling efficiency and the fluorescence excitation rate (Sinibaldi et al., 2014). The angularly resolved detection of either the reflected light (LF) or the fluorescent emission (FLR) is carried out by means of cylindrical optics and a CCD image sensor, with an angular detection range of 2.7 deg in LF and 8 deg in FLR mode (Sinibaldi et al., 2014). This configuration allows to interrogate in parallel up to 100 sensitive spots along a 6 mm region by means of an illumination laser strip.

In Fig. 2 (a), we show the reflectance map recorded by the CCD in the LF mode, when a 1DPC biochip without any surface functionalization (bare biochip) is mounted on the platform and the fluidic channel is filled with the running buffer, i.e., the Phosphate Buffered Saline (PBS 1×). The intensity along a spot shows a resonant dip at θ_{BSW} in correspondence of the resonant excitation of the TE polarized BSW at λ_{LF}. The angular position of the BSW resonance θ_{BSW}, which is tracked by means of a peak finder routine and a quadratic polynomial fit, may change due to either a change Δn_L of the refractive index of the external analyte or to the growth of a biological layer Δh_{BIO} at the surface of the biochip, according to:

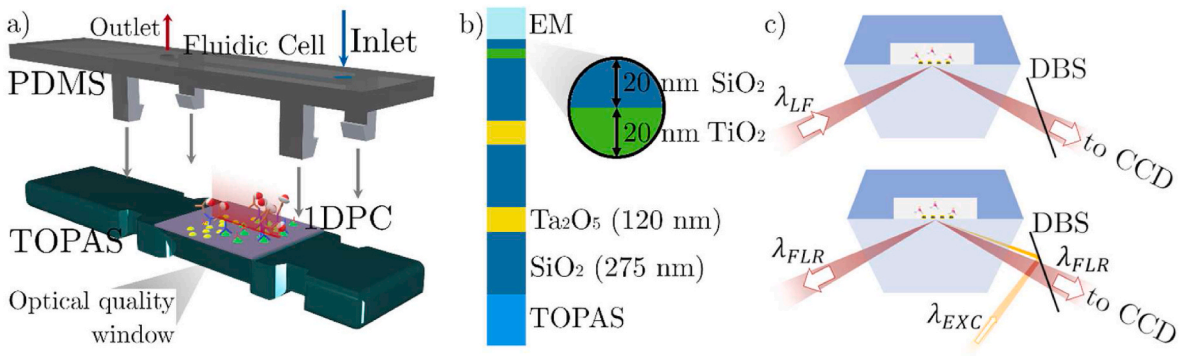

Fig. 1. (a) Schematic representation of the disposable biochip with its fluidic counterpart. (b) Sketch of the deposited 1DPC. (c) Sketch of the LF and FLR excitation and collection geometries.

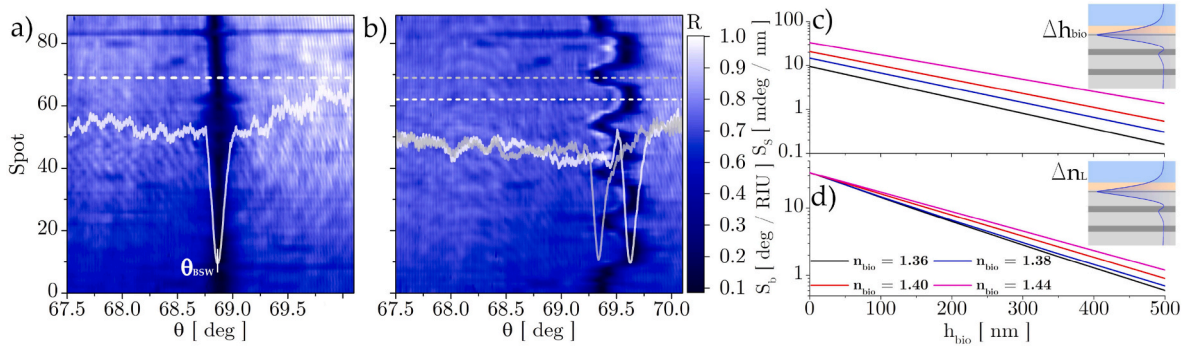

Fig. 2. (a,b) LF reflectance maps for a biochip filled with the running buffer. (a) bare biochip, (b) biochip after the injection and incubation of an undiluted positive (P) sample. We plot over the maps the reflected intensity along some specific spots along the illumination strip: (a) spot 69, (b) spot 69 within one CTRL zone (red dashed line) and spot 62 within the neighbouring SIG zone (white dashed line). θ_{BSW} is the angular position of the minimum of the dip. (c,d) Numerically calculated dependency of the surface sensitivity S_s (c) and of the bulk sensitivity S_b (d) as a function of the thickness of a biological layer adsorbed on top of the 1DPC, for four different values of the refractive index n_{bio} of the biolayer. (Insets) Calculated intensity profile of the TE polarized BSW and its penetration in the biolayer/liquid analyte effective medium. (For interpretation of the references to colour in this figure legend, the reader is referred to the Web version of this article.)

$$\Delta\theta_{BSW} = \left.\frac{\partial\theta_{BSW}}{\partial h_{BIO}}\right|_{n_L} \Delta h_{BIO} + \left.\frac{\partial\theta_{BSW}}{\partial n_L}\right|_{h_{BIO}} \Delta n_L = S_s \Delta h_{BIO} + S_b \Delta n_L \quad (1)$$

where S_s and S_b are generally referred to as surface and bulk sensitivities, respectively. The 1DPC and the LF read-out scheme were designed to maximize the surface sensitivity S_s.

In Fig. 2 (c), we show the plots of S_s of the 1DPC biochips as a function of h_{bio} and for different values of the refractive index n_{bio} of the biolayer, which can be estimated by using the Maxwell-Garnett mixing formula for different fractions of the filling material (water, n_L) into the matrix material that is a high-density packed proteins ($n = 1.44$) (Voros, 2004). The curves were numerically calculated by simulating the reflectance of the 1DPC structure by means of the transfer matrix method (Yeh and Yariv, 1978; Yeh, 1980), for increasing values of h_{bio}. They show that S_s decreases for increasing thickness of the adlayer and eventually vanishes for very high values, since the exponential tail of the BSW is less and less intense at the external sensitive interface. In the limit of small perturbations, S_s can be expressed as (Voros, 2004):

$$S_s = \frac{d\theta_{BSW}}{dh_{BIO}} = \frac{d\theta_{BSW}}{dn_{eff}} \frac{dn_{eff}}{dh_{BIO}} \approx S_b \frac{n_{BIO} - n_L}{L_P} \quad (2)$$

where n_{eff} is the effective refractive index probed by the BSW tail, L_P is the penetration depth of the BSW evanescent tail in the external medium, with $L_P \gg h_{BIO}$. The penetration depth is the distance from the surface at which the square modulus of the electric field is reduced by a factor of $1/e$ (Yeh et al., 1977).

Similarly to S_s, also S_b decreases for increasing h_{bio} values, as shown in Fig. 2 (d) for four different values of n_{bio}. For the bare 1DPC biochips, we measured $S_b = 34.0\ deg/RIU$ at λ_{LF} by means of calibration experiments carried out with a set of solutions with known refractive indices. Such value matches very well the theoretical value ($33.6\ deg/RIU$) at $h_{bio} = 0$ in Fig. 2 (d). Moreover, using the calculated value of $L_P = 113.5\ nm$, we could retrieve by means of Eq. (2) the S_s values in the low perturbation limit, which agree within 5% with those shown in Fig. 2 (c) for $h_{bio} = 0$.

2.3. Biochip bioconjugation

To efficiently bind the probe proteins onto the SiO_2 top layer surface of the disposable biochip, we utilized a silanization process based on (3 Aminopropyl)triethoxysilane (APTES) (Siva et al., 2014), along with glutaraldehyde (GA) as an organic homo-bifunctional crosslinker (further details in section S.3 of the SI) (Loudon, 2009). This procedure enables a high density of aldehydic groups on the sensitive surface of the biochip, which can be used to bioconjugate the proteins of interest.

Using a piezoelectric nano-plotter (Gesim), we dropped a solution of the RBD of the wild-type Spike protein (S-RBDwt, 26 kDa) in PBS 1× at a concentration of 100 $\mu g/mL$ (green region in Fig. 3 (a), step I). For each biochip, we plotted five separate sensitive regions (SIG, $\sim 560 \times 1250\ \mu m^2$ each) along the illumination laser strip and the microfluidic channel on the 1DPC surface (more details in section S.4 of the SI). The drops were then statically incubated for 1 h on a cold plate at 16.0 $°C$ in a controlled environment with a relative humidity $HR = 75\%$. In a practical application for a ready-to-use biochip, the functionalization would be completed by a blocking step, which involves incubating a bovine serum albumin (BSA, Sigma Aldrich) solution for a specified time to saturate the remaining reactive sites within and between the SIG regions. This process creates inert reference regions (CTRL) that separate the SIG ones. However, since we wanted to assess the bio-conjugation quality, we used the 1DPC biochip along with its microfluidic counterpart, as shown in Fig. 1 (a), and inserted it into the optical readout platform at this stage. The subsequent steps involved directly injecting solutions into the complete biochip at the beginning of the assays while monitoring the LF signal with the biochip mounted on the optical read-out system.

2.4. Human serum samples

Blood samples from a cohort of representative healthy donors and neoplastic patients previously infected by the SARS-CoV-2 were obtained from the IRCCS Regina Elena National Cancer Institute (IRE) Biobank after signing of a dedicated written informed consent. Whole blood has been processed within 1 h and sera were isolated by centrifugation at $2000 \times g$ for 20 min, and stored at $-80°C$ in single-use 0.5 mL aliquots with a unique and random barcode.

For each undiluted serum sample, the concentration was assessed by means of 2 different chemiluminescence immunoassay (CLIA) instruments, Maglumi 2019-nCoV IgG immunoassays (Snibe, threshold 1 AU/mL) and Liaison SARS-CoV-2 S1/S2 IgG assay (Diasorin, threshold 15 AU/mL). Two sera were selected, one negative (N, Maglumi 0.1 AU/mL, Liaison NA) and one positive (P, Maglumi 22.2 AU/mL, Liaison 383 AU/mL). The N serum was taken from a patient who had never been infected by the SARS-CoV-2. The P serum was taken from a patient who, at the time of sampling, had been infected by SARS-CoV-2, had recovered and had been tested negative for SARS-CoV-2 by PCR in the past 86 days.

For the assays carried out with the 1DPC biochips, both serum samples were either undiluted or diluted in a 0.1% solution of BSA in PBS 1×, at either 1:10 or 1:100.

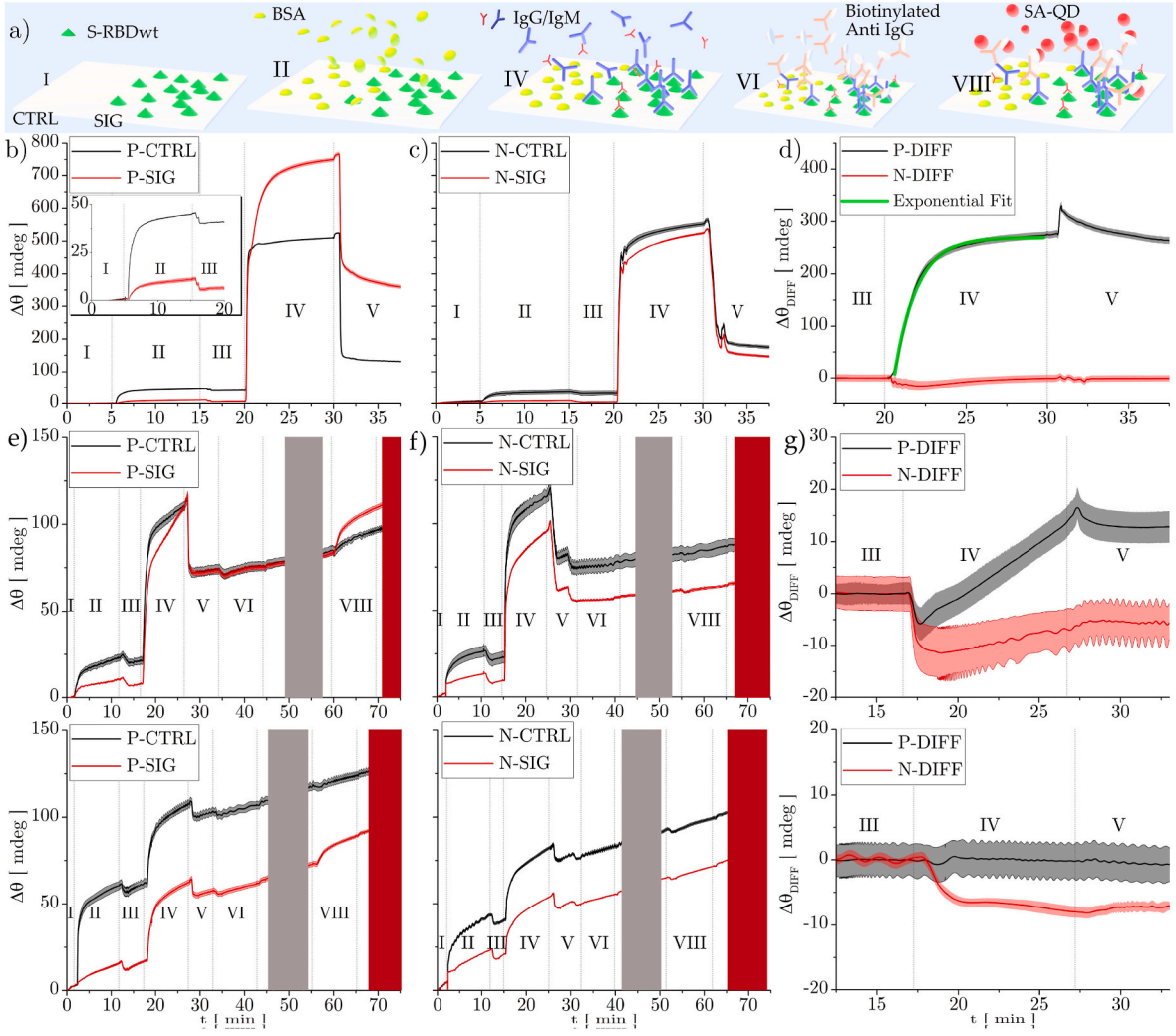

Fig. 3. (a) Immunoassay layout:(I) S-RBDwt immobilization in the SIG zone; (II) blocking with BSA; (IV) injection of the human serum and specific and non-specific capture of antibodies; (VI) injection and capture of the biotinylated anti-IgG detection antibodies; (VIII) injection and capture of the streptavidin-conjugated fluorescent quantum dots SA-QD; (III, V, VII, IX, not shown) washing steps with the running buffer. (b–c) LF sensograms recorded in assays with (b) positive (P) and (c) negative (N) undiluted samples. In the inset, we plot the magnified sensogram related to the biochip passivation (step II). (d) Differential sensograms obtained by subtracting the average curves recorded in adjacent SIG and CTRL regions for the P and N samples. The levels of the differential signals in the step III were set to zero. (e–f) LF sensograms recorded in assays carried out with either 1:10 (top) or 1:100 (bottom) diluted P (e) or N (f) human sera samples. g) Differential sensograms, calculated as in (d).

3. Results and discussion

3.1. Label-free detection

Fig. 3 (b) and (c) show the LF sensograms recorded during two assays carried out on different biochips with either the positive (P) or the negative (N) undiluted human sera, respectively. Each part of the LF assays, from I to V, corresponds to the biochemical steps shown in Fig. 3 (a), respectively. The sensograms report the shift $\Delta\theta$ of the BSW resonance with respect to the mean angular position measured in the running buffer during the step I. In each figure, the two experimental curves were recorded in either a SIG (red) or the neighbouring CTRL (black) region on the biochip surface. The curves where averaged over 8 statistically independent 67 μm wide spots, the minimum dimension of the spot (60 μm) being defined by the diffraction limit of the cylindrical spot imaging optics. The error bars are the standard deviation of the mean.

All assays started with a biochip filled with the running buffer PBS 1×. For any successive injection, we dispensed a volume $V_0 = 180\ \mu L$ at the flow rate $\Phi = 1.37\ \mu L/s$ by means of a motorized syringe pump (Tecan). The pump aspired the solutions from vials through a line including the biochip's microfluidic channel.

In the step II, a 0.1% solution of BSA in PBS 1× was injected and incubated for 10 min. The sensograms show that the BSA bound more efficiently to the CTRL region with respect to the SIG region, as for example in the inset of Fig. 3 (b). In Table 1, for all four combinations of samples and regions, we list the residual angular shift (RAS) $\Delta\theta_{BSW}$ measured after washing with the buffer (Fig. 3 (a) step III). For the washing step we used the pure buffer, without for example adding Tween 20 (Sinibaldi et al., 2020), in order to avoid the formation of microbubbles in the fluidic channel. Such a choice was maintained all over the assay. The far larger RAS recorded upon blocking with BSA in the initially bare CTRL region with respect to the SIG region confirms that a good surface coverage was reached during the S-RBDwt immobilization in the SIG regions.

In Table 1, we also list the thickness Δh_{BIO} of the adlayers, calculated by using the S_s curve shown in Fig. 2 (c) for $n_{bio} = 1.38$ and integrating to match the corresponding RAS as follows:

Table 1
–RAS values measured after washing in the running buffer after each injection/incubation step.

Dilution	Sample	Region	Step II		Step IV		Step VIII
			$\Delta\theta_{bsw}$ [mdeg]	Δh_{bio} [nm]	$\Delta\theta_{bsw}$ [mdeg]	Δh_{bio} [nm]	$\Delta\theta_{bsw}$ [mdeg]
undiluted	P	SIG	3.3 ± 0.2	0.2	410 ± 6	31.3	NA
		CTRL	35 ± 2	2.5	103 ± 6	7.0	NA
	N	SIG	−0.2 ± 0.2	−0.1	155 ± 7	11.0	NA
		CTRL	23 ± 2	1.5	156 ± 5	11.2	NA
1:10	P	SIG	−0.3 ± 0.2	−0.1	59 ± 2	4.0	19 ± 2
		CTRL	13 ± 2	1.0	47 ± 2	3.2	6 ± 2
	N	SIG	−0.3 ± 0.2	−0.1	45 ± 2	3.1	0
		CTRL	13 ± 2	1.0	50 ± 2	3.4	0
1:100	P	SIG	−4.2 ± 0.2	−0.3	24 ± 2	1.7	9 ± 2
		CTRL	41 ± 2	3.0	25 ± 2	1.5	0
	N	SIG	3.1 ± 0.2	0.2	16 ± 2	1.2	0
		CTRL	23 ± 2	1.5	28 ± 2	2.0	0

NOTE The protein biolayers' thickness Δh_{bio} was estimated assuming as mean refractive index n_{bio}= 1.38 and the error is omitted for the sake of clarity.

$$\Delta\theta_{BSW} = \int_0^{\Delta h_{BIO}} S_s(h)dh \tag{3}$$

The value found for the bare CTRL regions is in the range of the coverage expected for the dimensions of the BSA protein (Wright and Thompson, 1975). In conclusion, the sensing surface was patterned into five signal areas (SIG) and four intermediate control regions to be used as internal references (CTRL), as highlighted in Step III in Fig. 3 (a).

The injection of undiluted human serum samples gives rise to the $\Delta\theta_{BSW}$ kinetics recorded in step IV of Fig. 3 (b) and (c). In all cases, a steep shift of the BSW resonance angular position is observed, with the same amplitude ($\Delta\theta_{BSW} \cong 435 \pm 4\ mdeg$) in both the SIG and CTRL regions. Such shift is due to the contrast between the bulk refractive indices of the running buffer and of the serum. Since all regions started from the same coverage conditions with $h_{BIO} \cong 2.2 \pm 0.6\ nm$, which gives rise to an estimated $S_b \cong 33.1 \pm 0.2\ deg/RIU$, one can retrieve the bulk refractive index change as $\Delta n_L = \frac{\Delta\theta_{BSW}}{S_b} \cong (13.1 \pm 0.2) \bullet 10^{-3}$. In the case of the P sample, after the initial steep shift, the SIG and CTRL sensograms clearly show a different behaviour, demonstrating that an efficient capture of the anti-S antibodies took place in the SIG region. Washing with the running buffer in the step V, lead to the different RAS values listed in Table 1, which are partially due to both the specifically captured anti-SARS-CoV-2 Spike antibodies and to the non-specifically bound serum proteins. In the case of the N sample, Fig. 3 (c), the SIG and the CTRL sensograms exhibited the same kinetics and similar RAS values after the PBS 1× washing steps, indicating that no anti-SARS-CoV-2 Spike antibody was captured at the SIG region. Consistently, the RAS values recorded for the P sample in the CTRL region and for the N sample in both types of regions are in the same range, confirming that such RAS is due to non-specific binding of serum proteins all over the biochip sensitive surface.

In Fig. 3 (d), we show the differential sensograms $\Delta\theta_{DIFF}$ obtained by subtracting the average curves for the SIG and CTRL regions shown in Fig. 3 (b) and (c), for the P and the N sample, respectively. The curve for the N sample is almost flat, confirming that there was practically no differential response of the biosensor. The curve for the P sample shows a clear exponential behaviour, with a smooth start due to sample injection and diffusion, which cannot however be fitted with a single time constant. Such result demonstrates that the technique could and fastly discriminate patients' undiluted blood samples which were certified either positive or negative to SAR-CoV-2 antibodies. The detection time is $\tau_{DET} = 31\ s$, corresponding to the time when $\Delta\theta^P_{DIFF} - \Delta\theta^N_{DIFF} = 3\sigma_{DIFF}$, where σ_{DIFF} is the standard deviation of the $\Delta\theta^P_{DIFF} - \Delta\theta^N_{DIFF}$ signal.

The over-shoot signal $\Delta\theta_{OS} \cong 53 \pm 6\ mdeg$ observed for the P sample upon injection of the running buffer during the step V was due to the lack of compensation of the SIG and CTRL signals, since during the sample incubation they captured largely different quantities of anti-SARS-CoV-2 Spike antibodies and consequently their surface and bulk sensitivities changed with respect to each other. Assuming that the refractive index change is opposite ($-\Delta n_L$) with respect to that observed at the beginning of the step IV, we can estimate that $\Delta S_b = S_b^{CTRL} - S_b^{SIG} = \frac{\Delta\theta_{OS}}{\Delta n_L} = 4.1 \pm 0.5\ deg/RIU$. Such last value is consistent with the value that we can calculate from Fig. 2 (d), when using the measured RAS in the SIG and CTRL regions reported in Table 1, which is $\Delta S_b^{TH} = 4.7 \pm 0.5\ deg/RIU$.

The latter result indicates that the bulk sensitivity may vary by more than 10% during the assay with undiluted serum samples and large quantities of antibodies captured at the biochip surface and similarly the surface sensitivity. Such a drift of the sensitivities poses a concern on the possibility to retrieve any information on the association and dissociation constants from the fit of the exponential growth and decay observed in Fig. 3 (d). The drift might modify the shape of the curves from single exponential to multiple exponentials and the time constant values. As shown in Fig. 3 (d) by the green solid curve, the best single exponential fit matches only approximately the experimental data for the P serum sample with a time constant $\tau = (82.1 \pm 0.5)\ s$, with deviations that can be attributed to multiple exponential terms. However, we cannot exclude that such deviations originate from the sensitivity changes. It is therefore unlikely, under such conditions, to retrieve reliable values for the association and dissociation constants nor to distinguish between first-order and second order Langmuir processes, which appears to be very important issue for anti-SARS-CoV-2 Spike antibodies (Zhang et al., 2022).

Fig. 2 (b) shows the reflectance map acquired in the running buffer after the incubation of the undiluted P sample (Fig. 3 (a) step V). Clearly, at the end of the LF assay, the BSW resonant dip shifted by approximately the same amount in the 5 sensitive SIG regions. The bar chart in Fig. 4 compares the RAS recorded in the five SIG regions after the

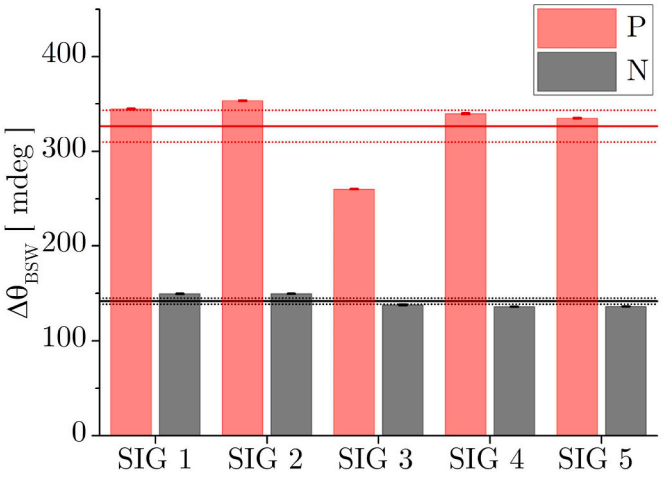

Fig. 4. RAS measured in the running buffer and in the five SIG regions of two different biochips after the incubation of either a P or a N serum sample. The solid and dashed lines are the mean over the five SIG regions and the dashed lines mark the std of the mean interval.

incubation of either the P or the N sample. The result demonstrates the good homogeneity of the response along the illumination strip and opens the way to applications in which several different probe proteins are spotted on the sensitive surface of the same biochip for a multiplexed operation.

Fig. 3 (e) and (f) show the LF sensograms recorded in assays carried out with both the P and N diluted serum samples for the 1:10 (top) and 1:100 (bottom) dilutions, respectively. The curves were obtained with the same procedures used for the undiluted serum samples. Since the anti-SARS-CoV-2 antibody concentration is smaller, the binding kinetics are slower, the dynamical range of the signals is smaller and the parasitic drifts, such as those related to temperature changes, are more evident. Such a result demonstrates the need for the differential operation with neighbouring SIG and CTRL regions on the same biochip, i.e., any thermal drift - approximately consistent across the entire biochip - is inherently eliminated. The RAS after each incubation step, for the two dilutions and for the two types of serum samples, are listed in Table 1. They were obtained by subtracting the slope of the curves due to the temperature drift. The analysis of the differential sensograms recorded up to the step V, Fig. 3 (g, top), and the related RAS values show that discrimination of the 1:10 diluted P and N serum samples can be concluded in about 10 min, within the same 3σ criterion described above. On the other hand, no conclusion can be drawn in LF mode for the 1:100 diluted serum samples, as shown Fig. 3 (g, bottom). For both dilutions, the differential curves recorded for the N serum sample show a lack of compensation of the SIG and CTRL signals, setting a limit to the LF resolution.

The LF assay was completed by the steps VI and VIII sketched in Fig. 3 (a), which were followed by the two washing steps VII and XI in the running buffer, giving rise to the sensograms shown for the diluted samples in Fig. 3 (e) and (f). During the step VI a solution of biotinylated anti-IgG detection antibodies in PBS $1\times$ (dilution ratio 1:20) was injected in the microfluidic channel and incubated for 10 min. The biotinylated anti-IgG were selected to specifically detect the anti-SARS-CoV-2 Spike IgG antibodies bound at the biochip surface during the step IV. During the step VIII a solution of streptavidin-conjugated fluorescent quantum dots (SA-QD) in PBS $1\times$ at the concentration 2 nM was injected in the microfluidic channel and incubated for 10 min. Due to the strong affinity of biotin and streptavidin, the procedure leads to the decoration of the biochip with fluorescent QD only within the regions were the anti-SARS-CoV-2 spike IgG antibodies were captured and detected by the biotinylated anti-IgG. We selected the size of the quantum dots (QD655, S^{QD}, ThermoFisher Scientific) to provide a fluorescence emission band peaked at $\lambda_{FLR} = 655\ nm$, which is inside the FLR detection window of the read-out platform.

The steps VI to IX (Fig. 3 (a)) constitute a prosecution of the LF assay and a part of the subsequent FLR endpoint assay. Owing to the large refractive index perturbation provided by the QD eventually captured at the sensitive surface during the step VIII, the platform operates in an amplified refractometric mode. In the following we shall refer to this mode as amplified LF mode, even if it isn't strictly correct since we use QD as labels. With such a notation we intend that the amplified LF mode does not make use of the fluorescence of the QD. Fig. 3 (e) shows that a QD amplified LF signal can be observed during the step VIII. The RAS after step VIII listed in Table 1 indicate that even at the 1:100 dilution the P and N serum samples can be clearly distinguished within a 3σ criterion. Therefore, by terminating the assay after the incubation of the SA-QD solution, it was possible to detect anti-SARS-CoV-2 Spike IgG antibodies in a 1:100 diluted serum sample taken from a patient recovered from Covid-19, 86 days after the last negative molecular swab. Of course, the cost of such increased detectivity is that the QD amplified LF assay must be carried out up to step IX and takes a longer time (about 50 min from the injection of the serum sample).

Binding of the SA-QD in assays with diluted sera gave rise to RAS that do not match with the dilution factor and was not even observed for the undiluted sera (more details in section S.5 of the SI). Such an effect cannot be ascribed to a lack of S_s that, for the maximum value of Δh_{bio} listed in Table 1 and according to Fig. 2 (c), might decrease at maximum by a factor 1.25. Instead, we attribute the effect to the high concentration of other serum proteins in the undiluted sera; during the incubation of the sample, they were non-specifically adsorbed and formed a thick layer at the surface, which completely shielded it from subsequent specific interactions. The shielding effect decreased upon dilution, as witnessed by the decreasing values of the RAS after the step IV listed in Table 1, and made that biotinylated anti-IgG detection took place and SA-QD binding could be consequently observed.

3.2. Fluorescence detection

As said, the injection and incubation of the SA-QD solution constituted the last step of the LF assay and it was a part of the endpoint FLR assay. The SA-QD solution injection was preceded by the fluorescence background acquisition, and it was followed by the fluorescence measurement, grey and red bands in Fig. 3 (e) and (f) respectively. In Fig. 5, we show the background subtracted fluorescence emission (BS-FLR) maps recorded by the CCD at the end of the assay after the SA-QD incubation in the running buffer, when resonantly exciting the BSW at λ_{EXC} and detecting the BSW coupled fluorescence around λ_{FLR}. In the FLR mode any thermal drift is anyhow taken into account, since the fluorescence excitation takes place always under resonant conditions. The maps were recorded for assays carried out with either P or N sera and for either the 1:10 or 1:100 dilution. They show that, for fixed resonant excitation laser conditions and CCD exposure time, weak fluorescence intensities are observed for the N sample at both dilutions, for the 1:10 diluted P sample, and for a blank sample constituted by a BSA solution in PBS $1\times$ at the concentration $1\ mg/mL$. Actually, the weak BS-FLR can be evidenced by increasing the CCD exposure, as shown in the insets of Fig. 5 (a) for the 1:10 diluted sera. On the other hand, a clear BS-FLR signal is observed in the SIG regions for the 1:100 diluted P serum, under the same conditions. As shown by the superimposed plot of the fluorescence intensity along one spot in Fig. 5 (b, top), the emitted radiation couples to both the TE (higher intensity peak) and TM (lower intensity peak) polarized BSW modes supported by the 1DPC. Therefore, the biochips unequivocally discriminate in the FLR mode a P sample from a N at the 1:100 dilution (Fig. 5 (b, bottom)) or a blank (Fig. 5 (c)).

We could not observe any BS-FLR signal in the assays carried out with undiluted sera, in agreement with the absence of any LF signal upon injection of the SA-QD solution (see section S.5 in the SI). Such observations support the conclusion that the absence of the QD amplified LF response is neither due to a lack of LF resolution nor to a saturation of the LF signal, but to the fact that the biotinylated detection anti-IgG, and consequently the SA-QD, was not captured at the surface due to the shielding of the highly concentrated serum proteins. In addition, the thickness of the serum proteins layer may reduce the coupling strength between the QD emitters and the BSW modes (Michelotti and Sepe, 2019; Sepe et al., 2019). Such last effect is confirmed by the fact that a larger FLR signal is observed at 1:100 dilution, suggesting that the captured QD, even if their surface density might be lower, are closer to the 1DPC surface and they better couple to the BSW modes.

In Fig. 5 (d), we also show the fluorescence emission intensity averaged over θ, as a function of the spot number along the biochip surface for FLR assays carried out with the P sample (black), N sample (red), and blank (blue). In the case of the P sample, the averaged FLR signal follows the spatial modulation induced by the S-RBDwt pattern, confirming the selectivity of the biochips for anti-SARS-CoV-2 antibodies. The mean intensity over the spots of the five SIG regions (black lines) can be in all cases distinguished from the N sample and blank, within the 3σ criterion. We attribute the variation of the mean over the SIG regions to the variability of the S-RBDwt immobilization procedure by means of the nano-plotter, which will have to be improved in our future work. The spatial modulation of the intensity recorded for the N

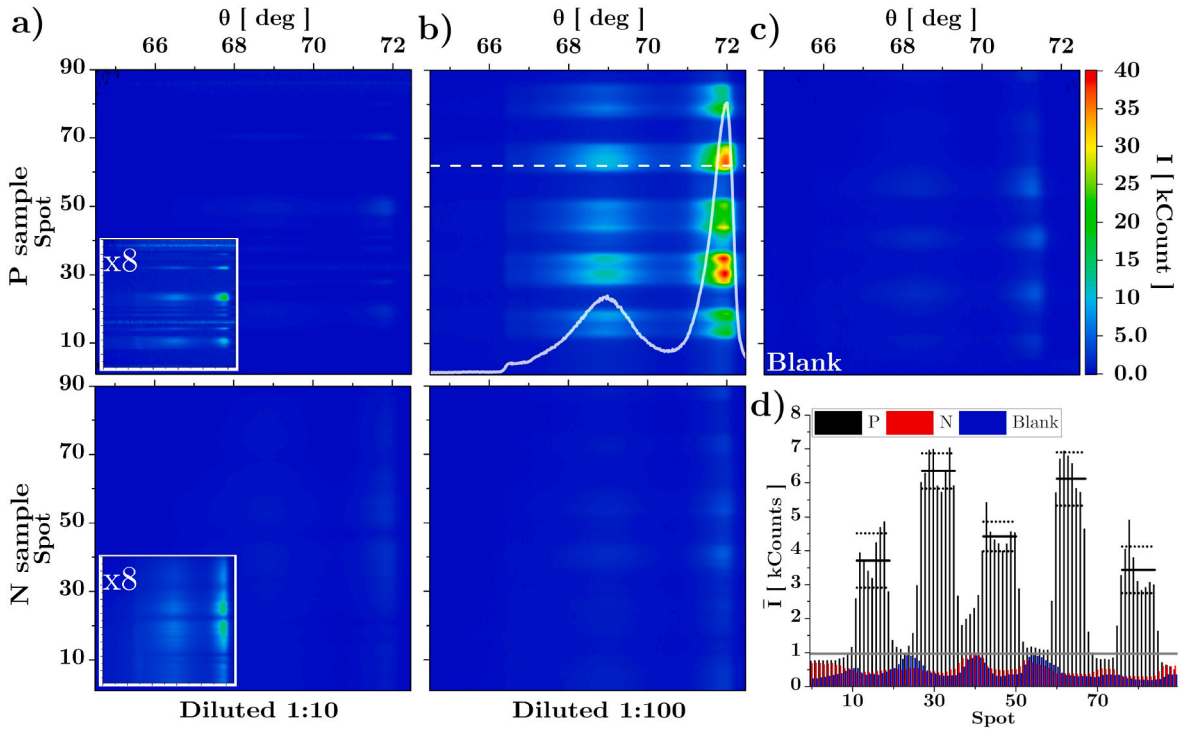

Fig. 5. (a–b) BS-FLR maps recorded under the same conditions in the FLUO mode at the end of assays carried out with either positive (top) or negative (bottom) sera: (a) 1:10 diluted sera; in the insets, we show the maps intensified by a factor 8; (b) 1:100 diluted sera. In the latter case, we superimpose over the map the plot of the fluorescence intensity along the spot 62. (c) BS-FLR maps for a blank sample. (d) Intensity collected from each of the 90 spots and averaged over the emission angular range, for 1:100 diluted P and N samples and for the blank; the black lines are the mean over the spots of the five SIG regions and the dashed lines the respective std intervals.

sample and the blank is phase-shifted and peaked in the CTRL regions. We attribute such an effect to the better anti-fouling properties of the SIG regions that are protected against non-specific binding by both BSA and the S-RBDwt.

Finally, the results show that the dynamic ranges of the biochip in the refractometric and fluorescence modes are disjoint. The refractometric mode can operate with both undiluted and 1:10 diluted sera, the QD amplified refractometric mode can operate with up to 1:100 diluted sera and the fluorescence mode can operate at dilutions equal or larger than 1:100.

4. Conclusions

In conclusion, we employed cost-effective disposable biochips featuring dielectric 1DPC layers on plastic substrates, enabling the propagation of BSW within the visible spectrum under TIR conditions. These biochips were designed to quantitatively identify specific proteins in aqueous solutions. The optical read-out system is a custom-made platform that combines both a refractometric and an end-point fluorescence operation mode, thereby enhancing sensitivity and selectivity.

The biochips were segmented into five distinct zones on their sensitive surface by means of a solution of S-RBDwt, after an initial process of surface silanization, and activation by means of glutaraldehyde crosslinking. Experimental outcomes in the refractometric operation mode displayed the biochips' ability to differentiate, in a label-free manner, serum samples from individuals tested positive or negative for anti-SARS-CoV-2 antibodies via chemiluminescent immunoassay (CLIA). This distinction was successful for both undiluted and 1:10 diluted sera, yielding detection times of approximately 31 s and 10 min, respectively. This validates the efficacy of the biochips and optical read-out system for antibody detection in a LF manner. The results from 1:10 diluted samples make it feasible to extract small volumes of serum, expanding their utility.

However, experiments revealed significant non-specific binding of serum proteins, leading to interference in the FLR read-out mode due to obscuration of the biochip's surface. Discrimination was achieved in FLR for 1:100 diluted samples, highlighting the potential for enhanced sensitivity in detecting anti-SARS-CoV-2 antibodies. This also indicated the possibility of extending the dynamic range for smaller antibody concentrations. The study's approach demonstrated promise for COVID-19 diagnostics, with potential applicability to other infectious diseases by adapting the assay format.

Notably, the LF mode's resolution rivaled that of commercial techniques, exhibiting even shorter detection times, particularly in undiluted samples. The future endeavours of the present study will explore the dynamic range of FLR for lower antibody concentrations by immobilizing different variants of Sars-CoV-2 spike protein. However, a comprehensive optimization exploring different functionalization and bio-conjugation routes and the construction of a reliable calibration curve are needed to transfer the technique in the clinical environment. Overall, this investigation underscores the potential of the proposed approach for sensitive and specific antibody detection, serving as a foundation for enhanced diagnostics in infectious diseases like COVID-19.

CRediT authorship contribution statement

Agostino Occhicone: Methodology, Software, Validation, Formal analysis, Investigation, Data curation, Writing – original draft, preparation. **Alberto Sinibaldi:** Conceptualization, Methodology, Validation, Investigation, Writing – original draft, preparation, Supervision, Project administration, Funding acquisition. **Daniele Chiappetta:** Methodology, Investigation. **Paola Di Matteo:** Methodology, Investigation. **Tommaso Pileri:** Methodology. **Norbert Danz:** Methodology, Software, Writing – review & editing. **Frank Sonntag:** Methodology, Resources. **Peter Munzert:** 1D-Photonic Crystals fabrication. **Matteo Allegretti:**

Conceptualization, Resources, Writing – review & editing, Supervision. **Valentina De Pascale:** Methodology, Investigation, preparation of serum samples. **Chiara Mandoj:** Resources, preparation of serum samples. **Francesco Michelotti:** Conceptualization, Methodology, Software, Formal analysis, Resources, Writing – original draft, preparation, Writing – review & editing, Supervision, Project administration, Funding acquisition.

Declaration of competing interest

The authors declare that they have no known competing financial interests or personal relationships that could have appeared to influence the work reported in this paper.

Data availability

Data will be made available on request.

Acknowledgements

A.O. acknowledges funding from the project BIOLIGHT (B86J20001690002), F.M. from the projects NANO-COVID-TEST (A0375-2020-36528) and PNRR-PNC-D34Health (B53C22006120001), A.S. from the projects ERBB2-2D (A0375-2020-36630), and PNRR-Rome Technopole Flagship Project 7 (B83C22002820006). The authors wish to thank Marco Magi for technical assistance.

Appendix A. Supplementary data

Supplementary data to this article can be found online at https://doi.org/10.1016/j.biosx.2023.100413.

References

Ascoli, C.A., 2021. Nat. Biotechnol. 39, 274–275. https://doi.org/10.1038/s41587-021-00845-3.
Chen, Y., Liu, F., Lee, L., 2022. Sci. Adv. 8 (21) https://doi.org/10.1126/sciadv.abn348.
Chen, Z., Zhang, Z., Zhai, X., Li, Y., Lin, L., Zhao, H., Bian, L., Li, P., Yu, L., Wu, Y., Lin, G., 2020. Anal. Chem. 92 (10), 7226–7231. https://doi.org/10.1021/acs.analchem.0c00784.
Choudhury, S., Badugu, R., Lakowicz, J., 2015. Acc. Chem. Res. 48, 2171–2180. https://doi.org/10.1021/acs.accounts.5b00100.
Coronaviridae Study Group of the International Committee on Taxonomy of Viruses, 2020. Nat. Microbiol. 5, 536–544. https://doi.org/10.1038/s41564-020-0695-z.
Danz, N., Kick, A., Sonntag, F., Schmieder, S., Höfer, B., Klotzbach, U., Mertig, M., 2011. Eng. Life Sci. 11, 566–572. https://doi.org/10.1002/elsc.201000192.
Degli-Eredi, I., Sipe, J., Vermeulen, N., 2018. Opt. Lett. 43, 1095. https://doi.org/10.1364/OL.43.001095.
Duffy, S., 2018. PLoS Biol. 16 (8) https://doi.org/10.1371/journal.pbio.3000003.
Farmer, A., Friedli, A., Wright, S., Robertson, W., 2012. Sensor. Actuator. B Chem. 173, 79–84. https://doi.org/10.1016/j.snb.2012.06.015.
Guo, Y., Divin, C., Myc, A., Terry, F., Baker, J., Norris, T., Yong Ye, J., 2008. Opt Express 16 (16), 11741–11749. https://doi.org/10.1364/OE.16.011741.
Guo, Y., Ye, J., Divin, C., Huang, B., Thomas, T., Baker, J., Norris, T., 2010. Anal. Chem. 82 (12), 5211–5218. https://doi.org/10.1021/ac100576y.
Han, T., Cong, H., Shen, Y., Yu, B., 2021. Talanta 233, 122609. https://doi.org/10.1016/j.talanta.2021.122609.
Homola, J., Yee, S., Gauglitz, G., 1999. Sensor. Actuator. B Chem. 54, 3–15. https://doi.org/10.1016/S0925-4005(98)00321-9.
Joannopoulos, J., Johnson, S., Winn, J., Meade, R., 2008. Photonic Crystals: Molding the Flow of Light. Princeton University press, Princeton and Oxford.
Kalas, B., Ferencz, K., Saftics, A., Czigany, Z., Fried, M., Petrik, P., 2021. Appl. Surf. Sci. 536 https://doi.org/10.1016/j.apsusc.2020.147869.
Konopsky, V., Alieva, E., 2007. Anal. Chem. 79 (12), 4729–4735. https://doi.org/10.1021/ac070275y.
Kretschmann, E., Raether, H., 1968. Z. Naturforsch. 23, 2135–2136. https://doi.org/10.1515/zna-1968-1247.
Lakowicz, J., 2006. Principles of Fluorescence Spectroscopy, third ed. Springer, New York. https://doi.org/10.1007/978-0-387-46312-4.
Lin, Q., Wen, D., Wu, J., Liu, L., Wu, W., Fang, X., Kong, J., 2020. Anal. Chem. 92 (14), 9454–9458. https://doi.org/10.1021/acs.analchem.0c01635.
Liscidini, M., Galli, M., Shi, M., Dacarro, G., Patrini, M., Bajoni, D., Sipe, J., 2009. Opt. Lett. 34, 2318–2320. https://doi.org/10.1364/OL.34.002318.
Liscidini, M., Sipe, J., 2007. Appl. Phys. Lett. 91 https://doi.org/10.1063/1.2826545, 253125.
Loudon, M., 2009. Organic Chemistry, fifth ed. Roberts and Company Publishers.
Mak, G., Cheng, P., Lau, S., Wong, K., Lau, C., Lam, E., Chan, R., Tsang, D., 2020. J. Clin. Virol. 129, 104500 https://doi.org/10.1016/j.jcv.2020.104500.
Meade, R., Brommer, K., Rappe, A., Joannopulos, J., 1991. Phys. Rev. B 44 (19), 10961–10964. https://doi.org/10.1103/PhysRevB.44.10961.
Michelotti, F., Dominici, L., Descrovi, E., Danz, N., Menchini, F., 2009. Opt. Lett. 34 (6), 839–841. https://doi.org/10.1364/OL.34.000839.
Michelotti, F., Sepe, E., 2019. J. Phys. Chem. C 123 (34), 21167–21175. https://doi.org/10.1021/acs.jpcc.9b05232.
Munzert, P., Danz, N., Sinibaldi, A., Michelotti, F., 2017. Surf. Coat. Technol. 314, 79–84. https://doi.org/10.1016/j.surfcoat.2016.08.029.
Naqvi, A., Fatima, K., Mohammad, T., Fatima, U., Singh, I., Singh, A., Muhammad Atif, S., Hariprasad, G., Hasan, G., Hassan, I., 2020. Biochim. Biophys. Acta, Mol. Basis Dis., 165878 https://doi.org/10.1016/j.bbadis.2020.165878, 1866.
Occhicone, A., Del Porto, P., Danz, N., Munzert, P., Sinibaldi, A., Michelotti, F., 2021. Crystals 11 (12), 1517. https://doi.org/10.3390/cryst11121517.
Paeder, V., Musi, V., Hvozdara, L., Herminjard, S., Herzig, H., 2011. Sensor. Actuator. B Chem. 157, 260–264. https://doi.org/10.1016/j.snb.2011.03.060.
Peeling, R., Olliaro, P., Boeras, D., Fongwen, N., 2021. Lancet Infect. Dis. 21 (9), e290–e295. https://doi.org/10.1016/S1473-3099(21)00048-7.
Perveen, S., Anjali Negi, A., Gopalakrishnan, V., Panda, S., Sharma, V., Sharma, R., 2023. Clin. Chim. Acta 538 (1), 139–156. https://doi.org/10.1016/j.cca.2022.11.017.
Petrova, I., Konopsky, V., Nabiev, I., Sukhanova, A., 2019. Sci. Rep. 9 https://doi.org/10.1038/s41598-019-45166-3.
Premkumar, L., Segovia-Chumbez, B., Jadi, R., Martinez, D., Raut, R., Markmann, A., Cornaby, C., Bartelt, L., Weiss, S., Park, Y., Edwards, C., Weimer, E., Scherer, E., Rouphael, N., Edupuganti, S., Weiskopf, D., Tse, L., Hou, Y., Margolis, D., Sette, A., Collins, M., Schmitz, J., Baric, R., de Silva, A., 2020. Sci. Immunol. 5, eabc8413 https://doi.org/10.1126/sciimmunol.abc8413.
Qiao, H., Guan, B., Gooding, J., Reece, P., 2010. Opt Express 18 (14), 15174–15182. https://doi.org/10.1364/OE.18.015174.
Raether, H., 1986. Surface Plasmons on Smooth and Rough Surfaces and on Gratings. Springer, Berlin.
Robertson, W., Wright, S., Friedli, A., Summers, J., Kaszynski, A., 2020. Biosens. Bioelectron. X, 5. https://doi.org/10.1016/j.biosx.2020.100049.
Rodriguez, G., Ryckman, J., Jiao, Y., Weiss, S., 2014. Biosens. Bioelectron. 53, 486–493. https://doi.org/10.1016/j.bios.2013.10.028.
Santi, S., Musi, V., Descrovi, E., Paeder, V., Di Francesco, J., Hvozdara, L., van der Wal, P., Lashuel, H.A., Pastore, A., Neier, R., Herzig, H., 2013. ChemPhysChem 14, 3476–3482. https://doi.org/10.1002/cphc.201300633.
Sepe, E., Sinibaldi, A., Danz, N., Munzert, P., Michelotti, F., 2019. J. Phys. Chem. C 123 (34), 21176–21184. https://doi.org/10.1021/acs.jpcc.9b05233.
Shafie, M., Dass, A., Shaberi, A., Zafarina, Z., 2023. Beni-Suef Univ. J. Basic Appl. Sci. 12 (6) https://doi.org/10.1186/s43088-023-00342-3.
Shinn, M., Robertson, W., 2005. Sensor. Actuator. B Chem. 105, 360–364. https://doi.org/10.1016/j.snb.2004.06.024.
Singhal, T., 2020. Indian J. Pediatr. 87 (4), 281–286. https://doi.org/10.1007/s12098-020-03263-6.
Sinibaldi, A., Danz, N., Anopchenko, A., Munzert, P., Schmieder, S., Chandrawati, R., Rizzo, R., Rana, S., Sonntag, F., Occhicone, A., Napione, L., De Panfilis, S., Stevens, M.M., Michelotti, F., 2015. J. Lightwave Technol. 33 (16), 3385–3393. https://doi.org/10.1109/JLT.2015.2448795.
Sinibaldi, A., Danz, N., Descrovi, E., Munzert, P., Schulz, U., Sonntag, F., Dominici, L., Michelotti, F., 2012. Sensor. Actuator. B Chem. 174 https://doi.org/10.1016/j.snb.2012.07.015.
Sinibaldi, A., Doricchi, A., Pileri, T., Allegretti, M., Danz, N., Munzert, P., Giordani, E., Giacomini, P., Michelotti, F., 2020. Anal. Bioanal. Chem. 412 (14) https://doi.org/10.1007/s00216-020-02643-3.
Sinibaldi, A., Fieramosca, A., Danz, N., Munzert, P., Occhicone, A., Barolo, C., Michelotti, F., 2018. J. Phys. Chem. C 122 (45), 26281–26287. https://doi.org/10.1021/acs.jpcc.8b09095.
Sinibaldi, A., Fieramosca, A., Rizzo, R., Anopchenko, A., Danz, N., Munzert, P., Magistris, C., Barolo, C., Michelotti, F., 2014. Opt. Lett. 39 (10), 2947–2950. https://doi.org/10.1364/OL.39.002947.
Sinibaldi, A., Rizzo, R., Figliozzi, G., Descrovi, E., Danz, N., Munzert, P., Anopchenko, A., Michelotti, F., 2013. Opt Express 21 (20), 23331–23344. https://doi.org/10.1364/OE.21.023331.
Sinibaldi, A., Sampaoli, C., Danz, N., Munzert, P., Sibilio, L., Sonntag, F., Occhicone, A., Falvo, E., Tremante, E., Giacomini, P., Michelotti, F., 2017. Biosens. Bioelectron. 92, 125–130. https://doi.org/10.1016/j.bios.2017.02.012.
Siva, N., Gunda, K., Singh, M., Norman, L., Kaur, K., Mitra, S., 2014. Appl. Surf. Sci. 305, 522–530. https://doi.org/10.1016/j.apsusc.2014.03.130.
Sreekanth, K., Zeng, S., Yong, K., Yu, T., 2013. Sensor. Actuator. B Chem. 182, 424–428. https://doi.org/10.1016/j.snb.2013.03.039.
Toma, K., Descrovi, E., Toma, M., Ballarini, M., Mandracci, P., Giorgis, F., Mateescu, A., Jonas, U., Knolla, W., Dostálek, J., 2013. Biosens. Bioelectron. 43, 108–114. https://doi.org/10.1016/j.bios.2012.12.001.
Vinogradov, A., Dorofeenko, A., Merzlikin, A., Lisyansky, A., 2010. Physics 53 (3), 243–256. https://doi.org/10.3367/UFNr.0180.201003b.0249.
Voros, J., 2004. Biophys. J. 87, 553–561. https://doi.org/10.1529/biophysj.103.030072.
WHO. (n.d. Retrieved 02 23, 2023, from. https://www.who.int/emergencies/diseases/novel-coronavirus-2019.
Wright, A., Thompson, M., 1975. Biophys. J. 15 (2), 137–141. https://doi.org/10.1016/S0006-3495(75)85797-3.
Ye, J., Ishikawa, M., Yamane, Y., Tsurumachi, N., 1999. Appl. Phys. Lett. 75, 3605–3607. https://doi.org/10.1063/1.125402.

Ye, J., Ishikawa, M., 2008. Opt. Lett. 33, 1729–1731. https://doi.org/10.1364/OL.33.001729.
Yeh, P., 1980. Surf. Sci. 96 (1–3), 41–53. https://doi.org/10.1016/0039-6028(80)90293-9.
Yeh, P., Yariv, A., 1978. Appl. Phys. Lett. 32 (2), 104–105. https://aip.scitation.org/doi/10.1063/1.89953.
Yeh, P., Yariv, A., Hong, C., 1977. J. Opt. Soc. Am. 67, 423–438. https://10.1364/JOSA.67.000423.
Yüce, M., Filiztekin, E., Özkaya, K., 2021. Biosens. Bioelectron. 172 (15), 112752 https://doi.org/10.1016/j.bios.2020.112752.
Zhang, M., Wang, H., Foster, E., Nikolov, Z., Fernando, S., King, M., 2022. Sci. Rep. 12 (789) https://doi.org/10.1038/s41598-021-04673-y.